A Computational Study of the Effects of Multiphase Dynamics in Catalytic Upgrading of Biomass Pyrolysis Vapor

Himanshu Goyal[1*], Olivier Desjardins[2], Perrine Pepiot[2], Jesse Capecelatro[3]

[1,*]Robert F. Smith School of Chemical and Biomolecular Engineering,

Cornell University, Ithaca, NY 14853, USA

[2]Sibley School of Mechanical and Aerospace Engineering,

Cornell University, Ithaca, NY 14853, USA

[3]Department of Mechanical Engineering,

University of Michigan, Ann Arbor, MI 48109, USA

Abstract

A recurring challenge among the variety of existing biomass-to-biofuel conversion technologies is the need to ensure optimal and homogeneous contact between the various phases involved. The formulation of robust design rules from an empirical standpoint alone remains difficult due to the wide range of granular flow regimes coexisting within a given reactor. In this work, a volume-filtered Eulerian-Lagrangian framework is employed that solves chemically reacting flows in the presence of catalytic particles. The simulation strategy is used to quantify the role of the particle clustering on catalytic upgrading of biomass pyrolysis vapor in risers. It is shown that particle clustering can reduce the catalytic conversion rate of biomass pyrolysis vapors by up to about 50%. The simulation results are also compared with an engineering model based on continuously stirred tank reactor (CSTR). A one-dimensional Reynolds-averaged transport equation is derived, and the unclosed terms that account for the heterogeneity caused by clusters are evaluated.

This is the author manuscript accepted for publication and has undergone full peer review but has not been through the copyediting, typesetting, pagination and proofreading process, which may lead to differences between this version and the Version of record. Please cite this article as doi:10.1002/aic.16184.

Introduction

In response to global climate change and society's continuously growing energy demand, there have been substantial efforts in recent years to reduce our dependence on fossil fuels and limit their associated environmental impacts. Many countries and regions have set aggressive goals for near-term deployment of second-generation biofuels derived from lignocellulosic biomass. By 2013, biofuel blend mandates were identified at the national level in 27 countries, and regulatory policies promoting the use of biofuels existed in more than 49 countries[1]. However, the high cost associated with efficient conversion of biomass to biofuel and the difficulties in developing new conversion processes make the large-scale commercialization of biofuels a significant challenge[2,3].

Among technologies for developing liquid biofuels derived from lignocellulosic biomass, thermochemical conversion techniques (e.g., gasification and pyrolysis) show great promise for being economically competitive with conventional petroleum derived gasoline and diesel[4,5,6]. In particular, the fast pyrolysis process in fluidized bed reactors is an emerging technology that can potentially yield liquids of up to 75% weight on a dry-feed basis[7,8]. The biomass volatile obtained from fast pyrolysis can be upgraded over a catalyst (e.g., zeolites or silica-alumina) prior to condensation for improving the compatibility of bio-oil with conventional processing infrastructure, yet this technology is still far from industrial application[9].

Catalytic upgrading of biomass is typically done in the riser of a circulating fluidized bed reactor (CFB), characterized by gas velocities greatly exceeding minimum fluidization. The high flow rates encountered in CFB risers cause the flow to become unsteady with large fluctuations in catalyst concentration. Local regions of densely packed catalytic particles, referred to as clusters, develop in the flow and fall at the walls of the reactor, while dilute suspensions of particles rise in the central region[10]. Clusters have been observed to reduce mixing and interaction of particles with the transport gas[11,12], potentially lowering operating efficiencies significantly. Meanwhile, detailed studies demonstrating the quantitative impact of particle clustering on chemical processes occurring in such flows remain elusive.

Because the solid phase is opaque and highly unsteady, experimental studies on the fluidiza-

tion of biomass have proven to be an arduous task[13]. In addition, the wide range of length and time scales associated with chemically reacting multiphase turbulence poses severe challenges in developing predictive models[14]. In recent years, computational fluid dynamics (CFD) has emerged as a promising tool to study the multiphase dynamic effects in practical pyrolysis reactors. Simulating catalytic conversion in fluidized bed reactors requires a kinetic model to describe the complex chemistry and a framework for solving gas-solid flows. The gas-solid description is typically computed using Eulerian-Eulerian (EE) or Eulerian-Lagrangian (EL) methods. EE representations solve the gas phase and solid particles on a common Eulerian grid, greatly reducing the computational cost as individual particles do not need to be tracked. In the limit where the flow is highly collisional and assumed to be nearly at equilibrium, the particle density function is close to Maxwellian and a Chapman-Enskog expansion can be used to derive a two-fluid model (TFM) using ensemble or volume averaging[15,16,17].

Lathouwers and Bellan[18] provided a comprehensive model for describing the thermofluid dynamics of dense, reactive, gas-solid mixtures to study the influence of operating parameters on tar yields during biomass pyrolysis. The equations were derived from the kinetic theory of granular flow and take into account multiple chemical reactions in both phases. In a more recent study, Xue et al.[19] combined TFM with a lumped, multi-component, multi-stage kinetic model. The model was used to simulate for the first time steady-state conditions of fast pyrolysis in a lab-scale fluidized-bed reactor. Within the last 15 years, the application of TFM to biomass pyrolysis has primarily focused on modeling dense two-dimensional bubbling fluidized bed reactors[18,20,19,21,22,23,24,25,26]. Lee et al.[27] recently performed several Euler-Euler simulations of biomass pyrolysis in three-dimensional bubbling fluidized beds to investigate the effect of bed geometry on biomass pyrolysis.

Due to the increased flow rates in CFB risers, the particle concentration becomes highly non-uniform and the velocity distribution deviates far from equilibrium. In this regime, particle trajectory crossings play an important role and higher moments of the particle number density must be considered to yield accurate results[28]. EL strategies provide an alternative

framework that typically rely on simpler closures compared to EE. With EL, individual particle trajectories are solved using Newton's laws of motion, and models are required for interphase exchange and particle collisions. Due to the added computational expense of tracking individual particles, EL methods coupled with a kinetic model have only recently been applied in three dimensions[29,30,12], and are generally limited to the dense granular flow regime near the inlet of the reactor. Most EL studies to date consider two-dimensional flows with a relatively small number of particles (e.g.,[31,32,33,34,35,36]). Recent work[37,38] has demonstrated that two-dimensional simulations are only capable of capturing qualitative features of particle clustering, and a fully three-dimensional description is required to accurately capture the quantitative flow behavior in CFB risers. Capecelatro et al.[12] performed three-dimensional EL simulations of catalytic particles in a periodic pipe flow. Those simulations showed that the presence of clusters delayed the conversion process by up to 85% compared to a corresponding homogeneous flow. However, the simulations did not account for spatial variations in the vertical direction that are known to have a large effect on biomass fast pyrolysis[39]. More details about CFD simulations of biomass pyrolysis can be found in a recent review by Xiong et al.[40].

In this study, we focus on characterizing and quantifying the effect of cluster formation on catalytic conversion in a three-dimensional CFB riser. The catalysts are representative of zeolites (e.g., HZSM-5), as they have been found to promote high yields of liquid products[8]. The EL approach is coupled with a simple kinetic model such that biomass vapors react with the catalytic particles to form light gases and cracked hydrocarbons. In section "Volume-filtered Euler-Lagrange approach", we present a volume-filtered EL approach for solving chemically reacting flows in the presence of solid particles, and provide a description of the corresponding numerical implementation. Simulation results are analyzed in section "Catalytic upgrading of volatile in a CFB riser". A comparison of simulation results with a representative engineering model is made in section "Reduced-order modeling". Finally, a reduced-order model based on Reynolds-averaging is proposed to account for the heterogeneity introduced by the multiphase dynamics in section "Reduced-order modeling". We are using SI units throughout the paper.

Volume-filtered Euler-Lagrange approach

The unsteady and multiscale nature of chemically reacting multiphase turbulence poses significant modeling challenges. In typical fluidized bed configurations for example, surface reactions and fluid instabilities taking place at the particle scale will ultimately influence the overall macroscopic behavior. Furthermore, the time scales associated with the reaction rates are often orders of magnitude smaller than the typical residence time of the gas phase. In order to formulate a system of equations that remain computationally tractable, a separation of length scales is established by introducing a local volume filter to the microscale (i.e., sub-particle scale) equations of motion[41,42]. To capture a significant portion of the small-scale features of the flow while enabling the use of classical models for microscale processes such as particle drag and mixture viscosity, the filter length scale δ_f should satisfy $d_p \ll \delta_f \ll \mathcal{L}$, where d_p is the particle diameter and $\mathcal{L}$ is a characteristic size of the mesoscale flow features (e.g., clusters). The corresponding volume-filtered EL equations are presented below. The reader is referred to Capecelatro et al.[42] for a more detailed description and complete derivation of those equations.

Gas-phase description

The volume-filtered continuity equation for a variable density flow is given by

$$\frac{\partial}{\partial t}\left(\varepsilon_f \rho_f\right) + \nabla \cdot \left(\varepsilon_f \rho_f \boldsymbol{u}_f\right) = 0. \tag{1}$$

where ε_f, ρ_f, and $\boldsymbol{u}_f$ are the volume-filtered fluid-phase volume fraction, density, and velocity, respectively. Here, we assume that catalytic coking does not become significant: therefore, the particle size remains constant. A comparison of the timescales for mass transfer between a particle and the surrounding gas and the gas-particle reaction shows that the mass transfer process is significantly faster than the catalytic reaction. Also, from the literature[43], for gas-porous catalyst system the mass transfer between the particle and the surrounding gas has negligible effect on the catalytic reaction. Hence, mass transfer resistance between the particle

and the surrounding gas is neglected. The volume-filtered fluid-phase momentum equation is given by

$$\frac{\partial}{\partial t}\left(\varepsilon_f \rho_f \boldsymbol{u}_f\right) + \nabla \cdot \left(\varepsilon_f \rho_f \boldsymbol{u}_f \otimes \boldsymbol{u}_f\right) = \nabla \cdot \left(\boldsymbol{\tau} - \boldsymbol{\mathcal{R}}_u\right) + \varepsilon_f \rho_f \boldsymbol{g} - \boldsymbol{F}^{\text{inter}}, \tag{2}$$

where $\boldsymbol{\tau}$ is the volume-filtered stress tensor, $\boldsymbol{\mathcal{R}}_u$ is akin to a Reynolds stress and requires closure, $\boldsymbol{g}$ is the gravity vector, and $\boldsymbol{F}^{\text{inter}}$ represents the interphase exchange between particles and the fluid, which will be made explicit in subsection "Interphase exchange". The isotropic part of sub-filter Reynolds stress term is absorbed in the fluid pressure p, whereas the anisotropic part is closed via a turbulent viscosity model, given by

$$\boldsymbol{\mathcal{R}}_u \approx \mu_t \left[\nabla \boldsymbol{u}_f + \nabla \boldsymbol{u}_f^{\mathsf{T}}\right], \tag{3}$$

where μ_t, analogous to a turbulent viscosity, is computed via a dynamic Smagorinsky model[44,45] based on Lagrangian averaging[46]. The volume-filtered fluid-phase stress tensor is expressed as

$$\boldsymbol{\tau} = -p\boldsymbol{I} + \left(\mu + \mu^*\right)\left[\nabla \boldsymbol{u}_f + \nabla \boldsymbol{u}_f^{\mathsf{T}} - \frac{2}{3}\left(\nabla \cdot \boldsymbol{u}_f\right)\boldsymbol{I}\right], \tag{4}$$

where $\boldsymbol{I}$ is the identity matrix, μ is the dynamic viscosity. The effective viscosity, μ^*, arises from filtering the velocity gradients in the microscale viscous stress tensor and accounts for enhanced dissipation by the particles. In this work, an effective viscosity derived by Gibilaro et al.[47] for fluidized beds is used, given by

$$\mu^* = \mu\left(\varepsilon_f^{-2.8} - 1\right). \tag{5}$$

Volume-filtered transport of reactive species i is given by

$$\frac{\partial}{\partial t}\left(\varepsilon_f \rho_f Y_i\right) + \nabla \cdot \left(\varepsilon_f \rho_f \boldsymbol{u}_f Y_i\right) = \nabla \cdot \left(\varepsilon_f \rho_f D_i \nabla Y_i - \boldsymbol{\mathcal{R}}_{Y_i}\right) + \dot{\omega}_i, \tag{6}$$

where Y_i is its mass fraction, D_i is its mass diffusivity, $\dot{\omega}_i$ is its filtered chemical source term, described in detail in the following section, and $\boldsymbol{\mathcal{R}}_{Y_i}$ is a sub-filtered scalar flux. In turbulent

combustion, closure for the sub-filter scalar flux is generally obtained by employing a gradient transport assumption and introducing a turbulent-like diffusivity D_t. Following Moin et al.[48], we introduce a dynamic formulation for D_t similar to the dynamic Smagorinsky model used in computing μ_t in Eq. (3).

The riser reactor is modeled as a vertical pipe with inlet and outlet boundary conditions. To account for the cylindrical geometry on a Cartesian mesh, a conservative immersed boundary (IB) method is employed. The IB method is based on a cut-cell formulation that requires rescaling of the convective and viscous fluxes in these cells[49]. At the reactor walls, no-slip and no penetration boundary conditions are used for the fluid and zero-gradient is enforced for the scalars.

Chemical kinetics for catalytic conversion

The kinetics of the catalytic conversion process are expected to have a significant impact on the quality and accuracy of the unsteady multiphase simulations, and therefore need to be modeled appropriately. However, the typical size of the reactor, even at laboratory scale, combined with the complexity of the associated multiphase flows, warrants the use of a highly lumped kinetic scheme. In this study, we assume that biomass vapors react with catalysts to form light gases and cracked hydrocarbons, according to a simple one-step reaction

$$\mathrm{VOL} + \mathrm{CAT} \longrightarrow \nu_{\mathrm{GAS}}\mathrm{GAS} + \nu_{\mathrm{HC}}\mathrm{HC} + \mathrm{CAT}, \tag{7}$$

where ν_i is the stoichiometric coefficient of species i, and the gas phase representative species, used to evaluate the gas mixture properties, are defined in Table 1. The reaction assumes that the catalytic conversion process is isothermal and catalyst particles do not deactivate. The reaction coefficient for the decomposition of biomass volatile is prescribed as

$$k = k_0 \frac{\varepsilon_p}{\varepsilon_{p,0}}, \tag{8}$$

where $\varepsilon_{p,0} = 0.634$ is the random close-packing limit for monodisperse spherical particles[50], and k_0 is chosen to obtain a specified conversion rate at the reactor exit. The consumption of biomass volatile is then obtained from the chemical source term

$$\dot{\omega}_i = \nu_i W_i k[\mathrm{VOL}], \tag{9}$$

where W_i is the molecular weight of species i, and the concentration of volatile is given by $[\mathrm{VOL}] = \varepsilon_f \rho_f Y_{\mathrm{VOL}}/W_{\mathrm{VOL}}$.

Particle-phase description

As described in the previous section, solid particles aid in the decomposition rate of biomass pyrolysis vapors to produce light gases (represented by CO) and cracked hydrocarbons (represented by toluene). In this work, the solid phase is treated in a Lagrangian framework, where individual particle trajectories are solved using Newton's second law of motion. Particles are represented as spheres of diameter d_p that are much denser than the surrounding fluid ($\rho_p \gg \rho_f$). The equations of motion for the particles are given by

$$\frac{d\boldsymbol{x}_p}{dt} = \boldsymbol{u}_p, \tag{10}$$

$$m_p \frac{d\boldsymbol{u}_p}{dt} = \boldsymbol{f}_p^{\mathrm{inter}} + \boldsymbol{F}_p^{\mathrm{col}} + m_p \boldsymbol{g}, \tag{11}$$

$$I_p \frac{d\boldsymbol{\omega}_p}{dt} = \sum_{j \neq p} \frac{d_p}{2} \boldsymbol{n} \times \boldsymbol{f}_{t,j\to p}^{\mathrm{col}}, \tag{12}$$

where $\boldsymbol{x}_p$ is the position of particle p, $\boldsymbol{u}_p$ is the particle velocity, $\boldsymbol{\omega}_p$, its angular velocity, $m_p = \pi \rho_p d_p^3/6$, its mass, and I_p, its moment of inertia given for a sphere by

$$I_p = \frac{m_p d_p^2}{10}. \tag{13}$$

In Eq. (11), $\boldsymbol{f}_p^{\text{inter}}$ is the force particle p experiences from the carrier fluid, as described in the following sub-section, and $\boldsymbol{F}_p^{\text{col}}$ is the collisional force that particle p experiences with adjacent particles and the walls. Particles rebound at the walls with a coefficient of restitution of 0.8. Collisions are handled via a soft-sphere approach originally proposed by Cundall and Strack[51]. Particle rotation is assumed to be only a function of the tangential component of the collision force, $\boldsymbol{f}_t^{\text{col}}$, that is solved based on the Coulomb friction law. Further details can be found in ref.[42].

Interphase exchange

Coupling between the gas phase and solid particles arise in the form of gas volume fraction ε_f and interphase exchange term $\boldsymbol{F}^{\text{inter}}$, expressed as

$$\varepsilon_p = 1 - \varepsilon_f \approx \sum_{p=1}^{N_p} G(|\boldsymbol{x} - \boldsymbol{x}_p|)\, V_p, \tag{14}$$

and

$$\boldsymbol{F}^{\text{inter}} \approx \sum_{p=1}^{N_p} G(|\boldsymbol{x} - \boldsymbol{x}_p|)\, \boldsymbol{f}_p^{\text{inter}}. \tag{15}$$

In the equations above, G is the filtering kernel taken to be Gaussian with a characteristic size $\delta_f = 8d_p$, and $\boldsymbol{f}_p^{\text{inter}}$ is given by

$$\boldsymbol{f}_p^{\text{inter}} \approx V_p \nabla \cdot \boldsymbol{\tau} + \boldsymbol{f}_p^{\text{drag}}, \tag{16}$$

with $\boldsymbol{f}_p^{\text{drag}}$ the drag force acting on the particle. The first term on the right-hand side of Eq. (16) represents contributions from the resolved fluid stresses that each particle experiences, and the last term accounts for the sub-filtered stresses in the form of drag that depends on the gas-phase velocity and volume fraction. The gas-phase variables are interpolated to the location of the particle via second-order trilinear interpolation and are used in the computation of the drag

force given by

$$\frac{\boldsymbol{f}_p^{\text{drag}}}{m_p} = \frac{\varepsilon_f}{\tau_p}(\boldsymbol{u}_f - \boldsymbol{u}_p)F(\varepsilon_f, \text{Re}_p), \tag{17}$$

where $\tau_p = \rho_p d_p^2/(18\mu)$ is the particle response time derived from a Stokes flow assumption, and the particle Reynolds number is given by

$$\text{Re}_p = \frac{\varepsilon_f \rho_f \left|\boldsymbol{u}_f - \boldsymbol{u}_p\right| d_p}{\mu}. \tag{18}$$

F is the dimensionless drag force coefficient of Tenneti et al.[52], which depends on the particle Reynolds number and fluid volume fraction experienced by the particle. An exhaustive description of the formulation can be found in ref.[42].

Numerical Implementation

The volume-filtered variable density equations are implemented in the framework of NGA[53], a fully conservative CFD code tailored for turbulent flow computations. The Navier-Stokes equations are solved on a staggered grid with second-order spatial accuracy for both the convective and viscous terms, and the second-order accurate semi-implicit Crank-Nicolson scheme of ref[54] is implemented for time advancement. The details on the mass, momentum, and energy conserving finite difference scheme are available in ref.[53].

The particles are distributed among the processors based on the underlying domain decomposition of the gas phase. For each particle, its position, velocity, and angular velocity are solved using a second-order Runge-Kutta scheme. To properly resolve the collisions without requiring an excessively small timestep, particles are restricted to move no more than one tenth of their diameter per timestep.

Catalytic upgrading of volatile in a CFB riser

Simulation configuration

Three-dimensional simulations are conducted to study catalytic upgrading of biomass in the CFB riser shown in Fig. 1. The catalysts are assumed to be spherical, with diameter $d_p = 100\mu$m, density $\rho_p = 875$ kg/m^3, both coefficient of restitution $e = 0.8$, and coefficient of friction $\mu_f = 0.1$ for particles and walls. The particles are initially uniformly distributed on a Cartesian lattice with a mean concentration $\bar{\varepsilon}_p = 0.05$, where $\bar{(\cdot)}$ denotes an average in space and time. The three-dimensional domain consists of $1024 \times 72 \times 72$ grid points and 1.16×10^6 particles. As catalytic particles leave the riser at the top, new particles are injected at the bottom cells such that the mean particle volume fraction in the reactor remains constant. We vary the reaction rate constant and the inlet gas-phase velocity, and consider three simulation cases, $\mathcal{S}1$, $\mathcal{S}2$, and $\mathcal{S}3$, with different combinations of reaction rate constant and inlet gas-phase velocity. The parameters are listed in Table 2. Simulations were carried out on 288 cores of the SDSC supercomputer Comet with Intel Xeon E5-2680v3 2.5 GHz cores. It required 55,000, 76,000, and 100,000 CPU hours for simulation cases $\mathcal{S}1$, $\mathcal{S}2$, and $\mathcal{S}3$, respectively to obtain converged statistics.

A note on dimensional analysis

We anticipate reduced mixing between the volatile and catalyst particles due to clustering, and the impact of this reduced mixing on the volatile conversion is linked to the Damköhler number, Da, defined as the ratio of reaction rate to mass transport rate occurring in the system. The base case reactor configuration, $\mathcal{S}1$, is calibrated such that a 90% conversion is achieved at the exit of the riser by fixing the reaction rate coefficient, k, under the assumption of flow homogeneity. Therefore, for a convection-dominated riser with an homogeneous particle distribution, the Damköhler number is

$$\mathrm{Da} = \frac{k}{U/H} \sim 1, \tag{19}$$

where H is the reactor height and U is the inflow velocity at the bottom of the riser. However, inhomogeneities are expected to develop within the reactor in the form of clusters. These clusters hinder mixing between the volatile and the particles. As we only consider the catalytic reaction between volatile and particles, the time scale associated with the transport of volatile into the clusters is expected to increase. Therefore, mesoscale processes in the reactor are characterized by a larger Damköhler number. As a result, the chemical kinetics are expected to be fast in comparison to the species transport within the reactor, suggesting that clusters will play an important role in the conversion process.

Another important dimensionless number is the axial Péclet number, Pe, that quantifies the extent of backmixing of the gas caused by the clusters falling near the riser walls. Pe is defined as the ratio of the advective flow to dispersive flow in the axial direction[55], given by

$$\mathrm{Pe} = \frac{HU}{\mathcal{D}}, \tag{20}$$

where $\mathcal{D}$ is the axial-dispersion coefficient. A large value of $\mathcal{D}$ corresponds to large backmixing of the gas, which is expected to negatively impact the volatile conversion. For the riser simulations considered in this work, we approximate $\mathcal{D}$/H as the downward moving gas velocity averaged over the entire riser, U_{downward}.

Results and discussion

Simulation results are gathered after the initial transient is complete and the flow reaches a statistically stationary state. From Fig. 2, the instantaneous flow is observed to be highly unsteady with large spatial inhomogeneity in particle concentration. A snapshot of particle position colored by the vertical component of particle velocity is given in Fig. 2(a). Particles tend to fall at the reactor wall and rise in the center, and the lateral distribution of volatile and hydrocarbons is observed to be strongly correlated with particle concentration. As seen in Figs. 2(c) and 2(d), the volatile is almost entirely depleted at the reactor wall resulting in a high concentration of hydrocarbons. Away from the wall, reduced contact of the volatile with

catalytic particles results in a low yield of hydrocarbons.

Figure 3 shows the mean particle concentration and mean species mass fractions along the reactor height for simulation cases $\mathcal{S}1$, $\mathcal{S}2$, and $\mathcal{S}3$. We can make the following comments:

- For $\mathcal{S}1$ and $\mathcal{S}2$, the particle concentration is maximum near the inlet, and reduces by more than an order of magnitude at the outlet. In $\mathcal{S}3$, however, the increased inflow velocity leads to significantly different bed hydrodynamics, with a more uniform axial distribution of particle concentration.

- Within five diameters of the inlet, most of the biomass volatile is converted into products for $\mathcal{S}1$ and $\mathcal{S}2$. Above this height, the conversion rate decreases and the species mass fractions remain approximately constant. In contrast, $\mathcal{S}3$ shows a continuous decrease in the biomass volatile up to the reactor outlet. Each riser is also modeled as an homogeneous reactor with reaction rate constant, k_0 and gas residence time, based on the riser height and the inlet gas velocity, same as that of the riser. In all cases, the volatile mass fractions at the outlet of the riser ($\mathcal{Y}^*_{\text{out}} = 0.131$ for $\mathcal{S}1$, 0.054 for $\mathcal{S}2$, and 0.185 for $\mathcal{S}3$) are observed to be higher than in the corresponding homogenous cases ($\mathcal{Y}_{\text{out}} = 0.05$ for $\mathcal{S}1$, 0.005 for $\mathcal{S}2$, and 0.158 for $\mathcal{S}3$). This discrepancy is attributed to the heterogeneity in the particle phase caused by the two-phase flow dynamics.

A more detailed picture of the riser dynamics can be obtained from the radial profiles at various locations of the riser. Figure 4 shows the radial profiles of the particle concentration normalized by its average over the cross-sectional area, and the volatile mass fraction at various reactor heights. Following observations can be made:

- A similar level of particle concentration inhomogeneity in the radial direction is observed for all simulation cases, with the particle concentration near the wall approximately twice the particle concentration at the center of the riser.

- For $\mathcal{S}1$ and $\mathcal{S}2$, the volatile is quickly depleted and reaches constant value near the riser wall. However, in the $\mathcal{S}3$ case, a continuous depletion of the volatile is observed near the

riser wall along the reactor height despite the radial distribution of the particle concentration being similar to $\mathcal{S}1$ and $\mathcal{S}2$. This suggests an enhanced mixing of the volatile between the riser core and the particle clusters due to higher inlet velocity in $\mathcal{S}3$.

In summary, a higher inlet velocity (in case $\mathcal{S}3$) significantly modifies the axial distribution of the particle phase, yet does not significantly impact its radial distribution. However, both the axial and radial profiles of the volatile mass fraction are significantly different for $\mathcal{S}3$ in comparison to $\mathcal{S}1$ and $\mathcal{S}2$. Another important effect of inlet velocity is observed on the backmixing of the gas. To quantify the backmixing, we calculate the average velocity of the downward moving gas, U_{downward}, which is found to be 0.12 m/s, 0.11 m/s, and 0.04 m/s for $\mathcal{S}1$, $\mathcal{S}2$, and $\mathcal{S}3$, respectively. It shows that higher inlet velocity significantly reduces the backmixing of the gas.

To further explore the role of the riser hydrodynamics on the catalytic conversion of the volatile, we introduce an effective reaction rate constant, k_0^*, corresponding to an homogeneous distribution of the particles with the same inlet and outlet volatile mass fractions as the risers simulated in cases $\mathcal{S}1$ to $\mathcal{S}3$.By integrating the rate equations for first order chemical kinetics in an homogeneous system and comparing the reaction rate constants:

$$k_0^* = k_0 \frac{\ln\left(\mathcal{Y}_{\text{out}}^*/\mathcal{Y}_{\text{in}}\right)}{\ln\left(\mathcal{Y}_{\text{out}}/\mathcal{Y}_{\text{in}}\right)}. \tag{21}$$

where $\mathcal{Y}_{\text{in}}$=0.5 is the inlet volatile mass fraction, $\mathcal{Y}_{\text{out}}$ is the outlet volatile mass fractions obtained from an homogeneous reactor using a reaction rate constant of k_0 as described above, and $\mathcal{Y}_{\text{out}}^*$ is the outlet volatile mass fraction of the riser observed in the simulation. The relevant parameters for calculating k_0^* are provided in Table 3. In each case, we find that $k_0^* < k_0$, demonstrating that the reduced mixing between the volatile and catalyst particles and backmixing of the gas due to clustering negatively impacts the catalytic conversion. This impact is quantified by a percentage reduction in reaction rate constant, $\mathcal{R}_{k_0} = (k_0 - k_0^*)/k_0^*$ shown in Table 3. For different simulation cases, the magnitude of $\mathcal{R}_{k_0}$ follows:

$$\mathcal{R}_{k_0,\mathcal{S}2} > \mathcal{R}_{k_0,\mathcal{S}1} > \mathcal{R}_{k_0,\mathcal{S}3}. \tag{22}$$

As shown in Table 3, $\mathcal{R}_{k_0}$ for $\mathcal{S}1$ and $\mathcal{S}2$ are close and much higher than $\mathcal{R}_{k_0}$ for $\mathcal{S}3$. The trend of $\mathcal{R}_{k_0}$ can be explained by the following observations:

- The calculated values of bulk Da are provided in Table 4 and follow

$$\mathrm{Da}_{\mathcal{S}2} > \mathrm{Da}_{\mathcal{S}1} > \mathrm{Da}_{\mathcal{S}3}. \tag{23}$$

  We expect the negative impact of clustering through the reduction of mixing between volatiles and particles to follow the same trend as Da.

- The calculated values of Pe are provided in Table 4 and follow

$$\mathrm{Pe}_{\mathcal{S}3} \gg \mathrm{Pe}_{\mathcal{S}1} \sim \mathrm{Pe}_{\mathcal{S}2}. \tag{24}$$

  This trend of Pe shows that backmixing of gas is much more prominent in $\mathcal{S}1$ and $\mathcal{S}2$ compared to $\mathcal{S}3$. Therefore, reduction in the volatile conversion should be much higher in $\mathcal{S}1$ and $\mathcal{S}2$ compared to $\mathcal{S}3$.

- As pointed out earlier, the axial distribution of particles is much more uniform in $\mathcal{S}3$ compared to $\mathcal{S}1$ and $\mathcal{S}2$, providing a better contact efficiency between the volatile and particles and higher volatile conversion in $\mathcal{S}3$.

These observations imply that an increase in velocity leads to a more homogeneous distribution of particles along the riser height and reduces the backmixing of the gas, leading to an improved volatile conversion.

Reduced-order modeling

Due to the excessive computational expense and time associated with simulating three-dimensional fluidized bed reactors, reduced-order models, often called engineering models, remain a key design tool for predicting the performance of multiphase reactors in a computationally affordable

manner. These models represent a simplified picture of the complex processes that happen in a multiphase reactor to reduce the computational expense. In literature, several papers[56,57,39,58] employ various engineering models to study biomass thermochemical conversion in fluidized bed reactors. In general, these models divide the fluidized bed reactor into several parts, such as bubble or emulsion phases, and use empirical models to represent each part. Another commonly employed strategy is to use one-dimensional conservation equations neglecting the unclosed terms. It remains a challenge to rigorously derive reduced-order models based on first principles. In the following subsections, we first compare the results of the three-dimensional riser simulations with a representative engineering model and show that the commonly used engineering models do not provide an adequate prediction of the three-dimensional simulation results. To remedy this, we rigorously derive a one-dimensional model by Reynolds-averaging the volume-filtered species conservation equation and validate it by comparing it with the predictions of our three-dimensional simulations.

Comparison with a representative engineering model

Engineering models typically employ a combination of plug flow reactors (PRFs) and/or continuously stirred reactors (CSTRs) to represent large-scale reactors at minimal cost. For example, Yan et al.[58] recently developed a one-dimensional model for biomass steam gasification in dual fluidized bed gasifiers using the commercial Aspen Plus software[59], where the riser was modeled as a series of CSTRs and the bubbling fluidized bed was modeled using a series of interacting PFRs and CSTRs. We want to assess the performance and predictive capabilities of such an engineering model for the riser considered in this work. We, therefore, model the riser as a series of n CSTRs, with n large enough to ensure smooth volatile mass fraction profiles. In the model, each CSTR is referred to as a stage in the riser. Following Yan et al.[58], neglecting axial and radial dispersion, the integral form of the molar balance equation for the riser model can be written as

$$M_{(i-1)} - A_{(i)}\varepsilon_{f,(i)} \int_{Z_{i-1}}^{Z_i} \Omega^j_{(i)} dZ - M_{(i)} = 0, \tag{25}$$

where the subscripts i and $i-1$ denote the outlet and inlet of stage i. $M_{(i)}$, $A_{(i)}$, and $\varepsilon_{f,(i)}$ denote the molar flow rate, the cross-sectional area, and the volume fraction of the gas phase in stage i, respectively. Z is the vertical coordinate and n is set to 20 in this case. $\Omega^j_{(i)}$ represents the consumption rate of species j in stage i. In this work, we take advantage of the detailed simulations performed in the previous section and use the $\varepsilon_{f,(i)}$ obtained from the detailed simulations directly. $\varepsilon_{f,(i)}$ being fully specified, Eq. (25) can be readily solved. The resulting volatile mass fraction profiles are compared with the three-dimensional simulations in Fig. 5. The percentage error in the prediction of the three-dimensional riser outlet volatile mass fraction using the engineering model is $\mathcal{E}_{\mathrm{VOL}} = 53\%$ for $\mathcal{S}1$, 83% for $\mathcal{S}2$, and 12% for $\mathcal{S}3$, even though the gas volume fraction is set to the correct value. In practice, however, this information is not available, and various empirical relations are typically used to evaluate $\varepsilon_{f,(i)}$ instead, whose lack of accuracy can further increase the deviation between the predictions of the riser simulations and the engineering model. The engineering model, therefore, appears not capable of satisfactorily predicting the three-dimensional simulation results, highlighting a need for more predictive, yet still computationally cheap models.

To move forward to improving on the CSTR-based engineering model, a one-dimensional model rigorously based on Reynolds-averaging the volume-filtered species conservation equations is presented in the following sub-section along with the closures for the resulting unclosed terms.

Reduced-order model development

Reynolds-averaged scalar transport equation

In order to develop a computationally inexpensive model for the catalytic conversion process in a riser, we Reynolds-average Eq. (6) in the angular direction and take cross-sectional average in the radial direction, which leads to a one-dimensional species transport equation in the axial

direction given by

$$\frac{\partial}{\partial t}\left(\langle\varepsilon_f\rho_f\rangle\widetilde{Y}_i\right)+\frac{\partial}{\partial x}\left(\langle\varepsilon_f\rho_f\rangle\widetilde{u_f}\widetilde{Y}_i\right)= -\frac{\partial}{\partial x}\left(\langle\varepsilon_f\rho_f\rangle\widetilde{u_f'Y_i'}\right)+\frac{\partial}{\partial x}\left(\langle\varepsilon_f\rho_f\rangle\widetilde{D_i\frac{\partial Y_i}{\partial x}}\right)+\langle\dot{\omega}_i\rangle, \tag{26}$$

with the chemical source term given by

$$\langle\dot{\omega}_i\rangle=\frac{\nu_i W_i k_0}{\varepsilon_{p,\max}W_{\mathrm{VOL}}}\langle\varepsilon_f\rho_f\rangle\left(\widetilde{\varepsilon}_p\widetilde{Y}_{\mathrm{VOL}}+\widetilde{\varepsilon_p'Y_{\mathrm{VOL}}'}\right). \tag{27}$$

In those equations, $\langle\cdot\rangle$ denotes a quantity averaged over the cross-sectional area and $\widetilde{(\cdot)}$ represents the density-weighted cross-sectional average known as Favre-average, i.e., $\widetilde{(\cdot)}=\langle(\cdot)\varepsilon_f\rho_f\rangle/\langle\varepsilon_f\rho_f\rangle$. $(\cdot)'$ denotes a fluctuation about a Favre-average quantity such that any variable can be decomposed into its density-weighted mean and fluctuation components, i.e., $(\cdot)=\widetilde{(\cdot)}+(\cdot)'$.

In Eq. (26), solving for $\widetilde{Y}_i$ requires closures for the unclosed terms, $\widetilde{u_f'Y_i'}$ and $\widetilde{\varepsilon_p'Y_{\mathrm{VOL}}'}$, on the right-hand side. The scalar flux term $\widetilde{u_f'Y_i'}$ arises from averaging the non-linear convective term in Eq. (6), and is expected to have a significant contribution due to strong lateral agitation created by the multiphase dynamics. Because the flow is convectively dominated, fluctuations about the Favre-average diffusion term $\widetilde{D_i\frac{\partial Y_i}{\partial x}}$ are expected to be small, and are therefore dropped from Eq. (26). The catalyst-volatile covariance term $\widetilde{\varepsilon_p'Y_{\mathrm{VOL}}'}$ in Eq. (27) accounts for lateral segregation in particle concentration as a result of clustering. A discussion of both the unclosed terms is provided in the next sub-section.

Analysis of the unclosed terms

Profiles of the unclosed terms appearing in Eqs. (26) and (27), $\widetilde{u_f'Y_i'}$ and $\widetilde{\varepsilon_p'Y_{\mathrm{VOL}}'}$, are shown in Fig. 6. Top row of Fig. 6 shows that $\widetilde{u_f'Y_{\mathrm{VOL}}'}$ is positive for all simulation cases, implying that the vertical component of the fluid velocity is positively correlated to volatile mass fraction. This can be explained by the fact that near the reactor inlet, the flow resembles that of a bubbling fluidized bed reactor, with strong recirculation and high level of mixing. A downward flow in this region

is indicative of increased interphase mixing and thus depletion of biomass volatile. Above the fluidized bed region, clusters fall at the walls and entrain the gas downward. Sustained contact between the phases within the clusters results in a low volatile mass fraction. The inverse is true for the products: gas and hydrocarbon. The covariances between the fluctuations of catalyst volume fraction and volatile mass fraction, $\widetilde{\varepsilon_p' Y_{\mathrm{VOL}}'}$, are found to be negative as shown in the bottom row of Fig. 6. It implies that an increase in local particle concentration corresponds to a depletion in the volatile mass fraction, with the greatest effect found near the reactor inlet. Near the exit, the volatile mass fraction and particle volume fraction are significantly lower, with their fluctuations nearly uncorrelated.

To correctly capture the two-phase dynamic effects on the conversion rate, the unclosed flux terms in Eqs. (26) and (27) need to be closed, that is, we need to develop models for them. Classical gradient diffusion models can be employed to model the scalar flux term ($\widetilde{u_f' Y_{\mathrm{VOL}}'}$). However, these models were designed for single-phase turbulence and are known to provide poor predictions in highly anisotropic flows[60]. We found that the mean scalar gradient is unable to reproduce the unclosed scalar flux profiles shown in Fig. 6, and thus more sophisticated models are needed. In Capecelatro et al.[12], an equation for $\widetilde{\varepsilon_p' Y_{\mathrm{VOL}}'}$ was derived for a zero-dimensional system. However, it was ultimately found that obtaining closures for the unclosed terms that appear in this equation for $\widetilde{\varepsilon_p' Y_{\mathrm{VOL}}'}$ is challenging.

The first step in deriving appropriate closures for $\widetilde{u_f' Y_i'}$ and $\widetilde{\varepsilon_p' Y_{\mathrm{VOL}}'}$, is to quantify their role in the dynamics of the system. For this purpose, the volatile mass fraction profiles obtained from the three-dimensional simulations $\mathcal{S}1$, $\mathcal{S}2$, and $\mathcal{S}3$, are compared with the profiles computed by solving Eq. (26) with

1. both unclosed terms neglected and $\widetilde{\varepsilon}_p$ taken to be constant (equal to $\overline{\varepsilon}_p$), and
2. both unclosed terms neglected and $\widetilde{\varepsilon}_p$ taken directly from the three-dimensional simulation.

The resulting volatile mass fraction profiles, displayed in Fig. 7, show that neglecting the unclosed terms ($\widetilde{u_f' Y_i'}$ and $\widetilde{\varepsilon_p' Y_{\mathrm{VOL}}'}$) results in an over-prediction of the conversion efficiency. The resulting

errors in the prediction of the outlet volatile mass fractions for $\mathcal{S}1$, $\mathcal{S}2$, and $\mathcal{S}3$ are $\mathcal{E}_{\mathrm{VOL}} = 62\%$, 91%, and 15% for the constant $\widetilde{\varepsilon}_p$ case, and $\mathcal{E}_{\mathrm{VOL}} = 56\%$, 88%, and 9% for the case where $\widetilde{\varepsilon}_p$ is obtained from the three-dimensional simulations. This demonstrates that Eq. (26) without the unclosed terms can not accurately predict the three-dimensional simulation results, even with the knowledge of particle concentration profile. This observation implies that those engineering models that do not accurately include the impact of heterogeneities in the riser will perform poorly even with an accurate knowledge of axial profiles of particle concentration and fluid velocity.

Next step in analyzing the role of the unclosed terms in the riser dynamics is to compare the impact of the individual unclosed terms on the one-dimensional model. For that, we compute the volatile mass fraction profiles by solving Eq. (26) with:

1. $\widetilde{u_f' Y_{\mathrm{VOL}}'}$ obtained from the three-dimensional simulations while neglecting $\widetilde{\varepsilon_p' Y_{\mathrm{VOL}}'}$, and
2. $\widetilde{\varepsilon_p' Y_{\mathrm{VOL}}'}$ obtained from the three-dimensional simulations while neglecting $\widetilde{u_f' Y_{\mathrm{VOL}}'}$

and compare them with the profiles obtained from the three-dimensional simulations in Fig. 8. Incorporating the scalar flux $\widetilde{u_f' Y_i'}$ obtained from the three-dimensional simulation significantly improves the prediction of the one-dimensional equation, whereas including $\widetilde{\varepsilon_p' Y_{\mathrm{VOL}}'}$ has a negligible effect on the prediction of the volatile mass fraction. This implies that lateral inhomogeneities due to clustering are impacting the catalytic conversion of volatile primarily through $\widetilde{u_f' Y_i'}$, and thus an accurate prediction of only $\widetilde{u_f' Y_i'}$ is sufficient to correctly capture the catalytic conversion process. This is done in the following sub-section.

Closure for the scalar flux $\widetilde{u_f' Y_{\mathrm{VOL}}'}$

We first quantify the strength of the correlation between u_f and Y_{VOL} by introducing the correlation coefficient $\rho_{X,Y}$ between two random variables X and Y:

$$\rho_{X,Y} = \frac{\widetilde{X'Y'}}{X_{\mathrm{RMS}} Y_{\mathrm{RMS}}}, \tag{28}$$

where $\widetilde{X'Y'}$ is the covariance of X and Y, and X_{RMS} and Y_{RMS} are the root-mean-square (RMS) of X' and Y', respectively. $\rho_{X,Y}$ being close to 1 implies that X and Y are strongly correlated and $\widetilde{X'Y'} \sim X_{\mathrm{RMS}} Y_{\mathrm{RMS}}$. Figure 9 shows that $\rho_{u_f,Y_{\mathrm{VOL}}}$ is close to 0.8 up to the riser height of x/D=11 in the $\mathcal{S}1$ and $\mathcal{S}2$ cases, whereas in the $\mathcal{S}3$ case, it is close to 0.9 for the entire length of the riser. Using $\rho_{u_f,Y_{\mathrm{VOL}}}$ equal to 1 in Eq. (28) for all simulation cases, we can model $\widetilde{u'_f Y'_{\mathrm{VOL}}}$ as

$$\left[\widetilde{u'_f Y'_{\mathrm{VOL}}}\right]_M = u_{f,\mathrm{RMS}} Y_{\mathrm{VOL,RMS}}, \tag{29}$$

where $\left[\widetilde{u'_f Y'_{\mathrm{VOL}}}\right]_M$ is the modeled value for $\widetilde{u'_f Y'_{\mathrm{VOL}}}$, and $u_{f,\mathrm{RMS}}$ and $Y_{\mathrm{VOL,RMS}}$ are the RMS values of u'_f and Y'_{VOL}, respectively. Figures 10(a), 11(a), and 12(a) compare $\left[\widetilde{u'_f Y'_{\mathrm{VOL}}}\right]_M$ with $\widetilde{u'_f Y'_{\mathrm{VOL}}}$ obtained from each of the three-dimensional simulations $\mathcal{S}1$, $\mathcal{S}2$, and $\mathcal{S}3$, indeed showing good agreement between the two.

To fully close this model, RMS variables now need to be defined in terms of the average variables $\widetilde{(\cdot)}$. $Y_{\mathrm{VOL,RMS}}$ is found to strongly follow the particle concentration profile, i.e., $Y_{\mathrm{VOL,RMS}} \approx \widetilde{\varepsilon}_p$, for $\mathcal{S}1$, $\mathcal{S}2$, and $\mathcal{S}3$, as shown in Figs. 10(b), 11(b), and 12(b). $u_{f,\mathrm{RMS}}$ strongly depends on the deviation of the axial fluid velocity across the riser cross-section from the mean axial fluid velocity, $\widetilde{u}_f$. Near the riser walls, gas gets trapped in the clusters and moves downward with falling clusters, significantly altering the gas velocity profile from the corresponding homogeneous case. It was found that $u_{f,\mathrm{RMS}}$ can be accurately computed if the cluster fall velocity, U_{cl}, is known. In the literature, models exist for U_{cl}, for example, that of Noymer and Glicksman[10]. Capecelatro et al.[37] performed simulations of a wall-bounded riser for a range of Archimedes numbers and showed that the cluster fall velocity follows the model developed by Noymer and Glicksman[10]. However, those simulations were periodic in the vertical direction and thus represented the fully developed region of a riser. In this work, the riser has strong heterogeneities in the vertical direction, thus the cluster fall velocity model of Noymer and Glicksman[10] can not be used here. In our knowledge, no analytical model exists that can accurately predict U_{cl} for a strongly heterogenous riser. Therefore, we make the additional assumption that the magnitude of $u_{f,RMS}$ is proportional to $\widetilde{u}_f$. Comparisons of $u_{f,RMS}$ and $\widetilde{u}_f$ for $\mathcal{S}1$, $\mathcal{S}2$, and $\mathcal{S}3$

are shown in Figs. 10(c), 11(c), and 12(c). Replacing $u_{f,RMS}$ with $\widetilde{u}_f$ and $Y_{\mathrm{VOL,RMS}}$ with $\widetilde{\varepsilon}_p$ in Eq. (29), $\widetilde{u'_f Y'_{\mathrm{VOL}}}$ is modeled as

$$\left[\widetilde{u'_f Y'_{\mathrm{VOL}}}\right]_M \approx \widetilde{u}_f \widetilde{\varepsilon}_p. \tag{30}$$

Figures 10(d), 11(d), and 12(d) compare $\widetilde{u'_f Y'_{\mathrm{VOL}}}$ with $\widetilde{u}_f \widetilde{\varepsilon}_p$ for $\mathcal{S}1$, $\mathcal{S}2$, and $\mathcal{S}3$ and show a good agreement between the two quantities. We therefore use $\widetilde{u}_f \widetilde{\varepsilon}_p$ as the model for $\widetilde{u'_f Y'_{\mathrm{VOL}}}$ in Eq.(26) and compare the computed volatile mass fraction profiles with the profiles obtained from the three-dimensional simulations shown in Fig. 13. An error $\mathcal{E}_{\mathrm{VOL}}$ of 7%, 21%, and 9% is obtained for the outlet volatile mass fractions for $\mathcal{S}1$, $\mathcal{S}2$, and $\mathcal{S}3$, respectively. It shows significant improvement in the predictions for $\mathcal{S}1$ and $\mathcal{S}2$, and preserves good performance for $\mathcal{S}3$.

Conclusions

In this work, three-dimensional simulations were conducted to assess the influence of multiphase dynamics on biomass pyrolysis vapor catalytic upgrading in risers. The catalytic bio-vapor conversion is represented by a single step reaction in a volume-filtered Euler-Lagrange framework. The riser reactor was operated with inlet velocities much higher than minimum fluidization velocity. Three simulation cases were considered with different combinations of reaction rate constant and inlet velocity, resulting in different Damköhler numbers. In each case, catalytic particles were observed to form clusters near the walls, resulting in strong heterogeneity in species concentration. This non-homogeneity was found to reduce the catalytic conversion rate of biomass pyrolysis vapors to hydrocarbons by up to 50%. Here, large Damköhler numbers were considered, such that the catalytic conversion process is limited by the mass transport process. Higher inlet gas velocity improved the catalytic conversion efficiency by enhancing the transport rate and reducing the backmixing of the gas. An engineering model was employed representing the riser as a series of continuously stirred tank reactors (CSTRs), and it was unable to reproduce the trends observed in the three-dimensional simulation. Instead, a one-

dimensional Reynolds-averaged transport equation was derived, and results were obtained by enforcing a uniform catalyst distribution (to model a homogeneous system) in addition to a mean catalyst distribution obtained from the three-dimensional simulations. In both cases, the model predictions of reactor outlet volatile mass fraction resulted in more than 50% error for lower inlet velocity simulations. The non-homogeneity causing this discrepancy was found to be completely captured in the turbulent scalar flux. By including this term, the one-dimensional model was able to reproduce the trends observed in the three-dimensional simulation.

The current conversion model does not account for catalyst deactivation, although this phenomenon is known to be of great importance when operating catalytic reactors. Looking forward, it would be necessary to account for deactivation for catalytic particles that have been exposed to volatile for a sufficiently long period of time. Accounting for this effect is likely to further reduce the conversion efficiency of the reactor, and further amplify the role played by clusters.

Acknowledgements

The authors gratefully acknowledge funding support provided by the National Science Foundation under Grants CBET 1437903 and CBET 1638837.

Literature Cited

1 REN21. Renewables 2013 Global Status Report. *Paris: REN21 Secretariat*. 2013;.

2 Chum H, Faaij A, Moreira J, Junginger H, Patel M. *IPCC special report on renewable energy sources and climate change mitigation*. Cambridge University Press. 2011.

3 Fiorese G, Catenacci M, Verdolini E, Bosetti V. Advanced biofuels: Future perspectives from an expert elicitation survey. *Energy Policy*. 2013;56:293–311.

4 Demirbas A. Progress and recent trends in biofuels. *Progress in energy and combustion science*. 2007;33(1):1–18.

5 Wright MM, Brown RC. Comparative economics of biorefineries based on the biochemical and thermochemical platforms. *Biofuels, Bioproducts and Biorefining*. 2007;1(1):49–56.

6 Foust T, Wallace R, Wooley R, Sheehan J, Ibsen K, Dayton D. A National Laboratory market and technology assessment of the 30x30 scenario. *Tech. Rep. TP-510-40942*, NREL. 2007.

7 Bridgwater A, Czernik S, Piskorz J. An overview of fast pyrolysis. *Progress in thermochemical biomass conversion*. 2001;pp. 977–997.

8 Bridgwater A. Review of fast pyrolysis of biomass and product upgrading. *Biomass and Bioenergy*. 2012;38:68–94.

9 Mortensen PM, Grunwaldt J, Jensen P, Knudsen K, Jensen A. A review of catalytic upgrading of bio-oil to engine fuels. *Applied Catalysis A: General*. 2011;407(1):1–19.

0 Noymer PD, Glicksman LR. Descent velocities of particle clusters at the wall of a circulating fluidized bed. *Chemical Engineering Science*. 2000;55(22):5283–5289.

1 Shaffer F, Gopalan B, Breault RW, Cocco R, Karri S, Hays R, Knowlton T. High speed imaging of particle flow fields in CFB risers. *Powder Technology*. 2013;.

2 Capecelatro J, Pepiot P, Desjardins O. Numerical investigation and modeling of reacting gas-solid flows in the presence of clusters. *Chemical Engineering Science*. 2015;122:403–415.

3 Cui H, Grace JR. Fluidization of biomass particles: A review of experimental multiphase flow aspects. *Chemical Engineering Science*. 2007;62(1):45–55.

4 Pepiot P, Dibble C, Foust T. Computational fluid dynamics modeling of biomass gasification and pyrolysis. In: *Computational modeling in lignocellulosic biofuel production. ACS symposium series*, vol. 1052. 2010; pp. 273–98.

5 Gidaspow D. *Multiphase flow and fluidization: continuum and kinetic theory descriptions*. Academic Pr. 1994.

6 Zhang D, Prosperetti A. Averaged equations for inviscid disperse two-phase flow. *Journal of Fluid Mechanics*. 1994;267:185–220.

7 Peirano E, Leckner B. Fundamentals of turbulent gas-solid flows applied to circulating fluidized bed combustion. *Progress in Energy and Combustion Science*. 1998;24(4):259–296.

8 Lathouwers D, Bellan J. Modeling of dense gas–solid reactive mixtures applied to biomass pyrolysis in a fluidized bed. *International Journal of Multiphase Flow*. 2001;27(12):2155–2187.

9 Xue Q, Heindel T, Fox R. A CFD model for biomass fast pyrolysis in fluidized-bed reactors. *Chemical Engineering Science*. 2011;66(11):2440–2452.

0 Gerhauser H, Generalis S, Hague R, Bridgwater A. CFD for the Modelling of Entrainment in Fluidised Bed Fast Pyrolysis of Biomass. *Progress in Thermochemical Biomass Conversion*. 2001;pp. 1281–1295.

1 Xue Q, Dalluge D, Heindel T, Fox R, Brown R. Experimental validation and CFD modeling study of biomass fast pyrolysis in fluidized-bed reactors. *Fuel*. 2012;97:757–769.

2 Xue Q, Fox R. Reprint of: Multi-fluid CFD modeling of biomass gasification in polydisperse fluidized-bed gasifiers. *Powder Technology*. 2014;265:23–34.

3 Xiong Q, Kong SC. Modeling effects of interphase transport coefficients on biomass pyrolysis in fluidized beds. *Powder Technology*. 2014;262:96–105.

4 Zhong H, Zhang J, Zhu Y, Liang S. Multi-fluid Modeling Biomass Fast Pyrolysis in the Fluidized-Bed Reactor Including Particle Shrinkage Effects. *Energy and Fuels*. 2016; 30(8):6440–6447.

5 Peng J, Eri Q, Zhao X. Detailed simulations of fast pyrolysis of biomass in a fluidized bed reactor. *Journal of Renewable and Sustainable Energy*. 2018;10(1):013104.

6 Brandão FL, Verissimo GL, Haikal Leite MA, Leiroz AJ, Cruz ME. Computational Study of Sugarcane Bagasse Pyrolysis Modeling in a Bubbling Fluidized Bed Reactor. *Energy & Fuels*. 2018;.

7 Lee JE, Park HC, Choi HS. Numerical Study on Fast Pyrolysis of Lignocellulosic Biomass with Varying Column Size of Bubbling Fluidized Bed. *ACS Sustainable Chemistry & Engineering*. 2017;5(3):2196–2204.

8 Desjardins O, Fox R, Villedieu P. A quadrature-based moment method for dilute fluid-particle flows. *Journal of Computational Physics*. 2008;227(4):2514–2539.

9 Bruchmüller J, van Wachem B, Gu S, Luo K, Brown R. Modeling the thermochemical degradation of biomass inside a fast pyrolysis fluidized bed reactor. *AIChE Journal*. 2012; 58(10):3030–3042.

0 Loha C, Chattopadhyay H, Chatterjee PK. Three dimensional kinetic modeling of fluidized bed biomass gasification. *Chemical Engineering Science*. 2014;109:53–64.

1 Fletcher D, Haynes B, Christo F, Joseph S. A CFD based combustion model of an entrained flow biomass gasifier. *Applied mathematical modelling*. 2000;24(3):165–182.

2 Papadikis K, Gu S, Bridgwater AV, Gerhauser H. Application of CFD to model fast pyrolysis of biomass. *Fuel Processing Technology*. 2009;90(4):504–512.

3 Oevermann M, Gerber S, Behrendt F. Euler–Lagrange/DEM simulation of wood gasification in a bubbling fluidized bed reactor. *Particuology*. 2009;7(4):307–316.

4 Rabinovich O, Borodulya V, Vinogradov L, Korban V. Fast pyrolysis of an ensemble of biomass particles in a fluidized bed. *Journal of Engineering Physics and Thermophysics*. 2010;83(4):742–752.

5 Goyal H, Pepiot P. Integrating Intra-Particle Processes in Large Scale Simulation of Biomass Thermochemical Conversion. In: *9th US Combustion Meeting, Cincinnati, Ohio*. 2015; .

6 Goyal H, Pepiot P. A compact kinetic model for biomass pyrolysis at gasification conditions. *Energy & Fuels*. 2017;31(11):12120–12132.

7 Capecelatro J, Pepiot P, Desjardins O. Numerical characterization and modeling of particle clustering in wall-bounded vertical risers. *Chem Eng J*. 2014;245:295–310.

8 Li T, Pannala S, Shahnam M. CFD simulations of circulating fluidized bed risers, part II, evaluation of differences between 2D and 3D simulations. *Powder Technology*. 2014;254:115–124.

9 Trendewicz A, Braun R, Dutta A, Ziegler J. One dimensional steady-state circulating fluidized-bed reactor model for biomass fast pyrolysis. *Fuel*. 2014;133:253–262.

0 Xiong Q, Yang Y, Xu F, Pan Y, Zhang J, Hong K, Lorenzini G, Wang S. Overview of computational fluid dynamics simulation of reactor-scale biomass pyrolysis. *ACS Sustainable Chemistry & Engineering*. 2017;5(4):2783–2798.

1 Anderson T, Jackson R. Fluid mechanical description of fluidized beds. Equations of motion. *Industrial & Engineering Chemistry Fundamentals*. 1967;6(4):527–539.

2 Capecelatro J, Desjardins O. An Euler-Lagrange strategy for simulating particle-laden flows. *Journal of Computational Physics*. 2013;238:1–31.

3 Levenspiel O. Chemical reaction engineering. *Industrial & engineering chemistry research*. 1999;38(11):4140–4143.

4 Germano M, Piomelli U, Moin P, Cabot WH. A dynamic subgrid-scale eddy viscosity model. *Physics of Fluids A: Fluid Dynamics*. 1991;3:1760.

5 Lilly D. A proposed modification of the Germano subgrid-scale closure method. *Physics of Fluids A: Fluid Dynamics*. 1992;4:633.

6 Meneveau C, Lund T, Cabot W. A Lagrangian dynamic subgrid-scale model of turbulence. *Journal of Fluid Mechanics*. 1996;319(1):353–385.

7 Gibilaro L, Gallucci K, Di Felice R, Pagliai P. On the apparent viscosity of a fluidized bed. *Chemical Engineering Science*. 2007;62(1-2):294–300.

8 Moin Pa, Squires K, Cabot W, Lee S. A dynamic subgrid-scale model for compressible turbulence and scalar transport. *Physics of Fluids A: Fluid Dynamics*. 1991;3(11):2746–2757.

9 Meyer M, Devesa A, Hickel S, Hu X, Adams N. A conservative immersed interface method for Large-Eddy Simulation of incompressible flows. *Journal of Computational Physics*. 2010; 229(18):6300–6317.

0 Scott G, Kilgour D. The density of random close packing of spheres. *Journal of Physics D: Applied Physics*. 1969;2:863.

1 Cundall P, Strack O. A discrete numerical model for granular assemblies. *Geotechnique*. 1979;29(1):47–65.

2 Tenneti S, Garg R, Subramaniam S. Drag law for monodisperse gas-solid systems using particle-resolved direct numerical simulation of flow past fixed assemblies of spheres. *International Journal of Multiphase Flow*. 2011;37(9):1072–1092.

3 Desjardins O, Blanquart G, Balarac G, Pitsch H. High order conservative finite difference scheme for variable density low Mach number turbulent flows. *Journal of Computational Physics*. 2008;227(15):7125–7159.

4 Pierce C. Progress-variable approach for large-eddy simulation of turbulent combustion. Ph.D. thesis, Stanford University. 2001.

5 Davis ME, Davis RJ. *Fundamentals of chemical reaction engineering*. Courier Corporation. 2012.

6 Sadaka SS, Ghaly A, Sabbah M. Two phase biomass air-steam gasification model for fluidized bed reactors: Part Imodel development. *Biomass and bioenergy*. 2002;22(6):439–462.

7 Nikoo MB, Mahinpey N. Simulation of biomass gasification in fluidized bed reactor using ASPEN PLUS. *Biomass and Bioenergy*. 2008;32(12):1245–1254.

8 Yan L, Lim CJ, Yue G, He B, Grace JR. One-dimensional modeling of a dual fluidized bed for biomass steam gasification. *Energy Conversion and Management*. 2016;127:612–622.

9 Plus A. Aspen Technology Inc. *Cambridge, MA, USA*. 2006;.

0 Combest DP, Ramachandran PA, Dudukovic MP. On the gradient diffusion hypothesis and passive scalar transport in turbulent flows. *Industrial & Engineering Chemistry Research*. 2011;50(15):8817–8823.

1 Adjaye JD, Bakhshi NN. Catalytic conversion of a biomass-derived oil to fuels and chemicals 1: model compound studies and reaction pathways. *Biomass and Bioenergy*. 1995;8(3):131–149.

2 Adjaye JD, Bakhshi NN. Catalytic conversion of a biomass-derived oil to fuels and chemicals 2: Chemical kinetics, parameter estimation and model predictions. *Biomass and Bioenergy*. 1995;8(4):265–277.

List of Figures

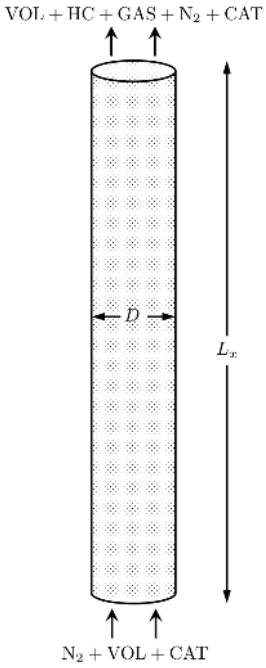

Figure 1: Three-dimensional riser configuration.

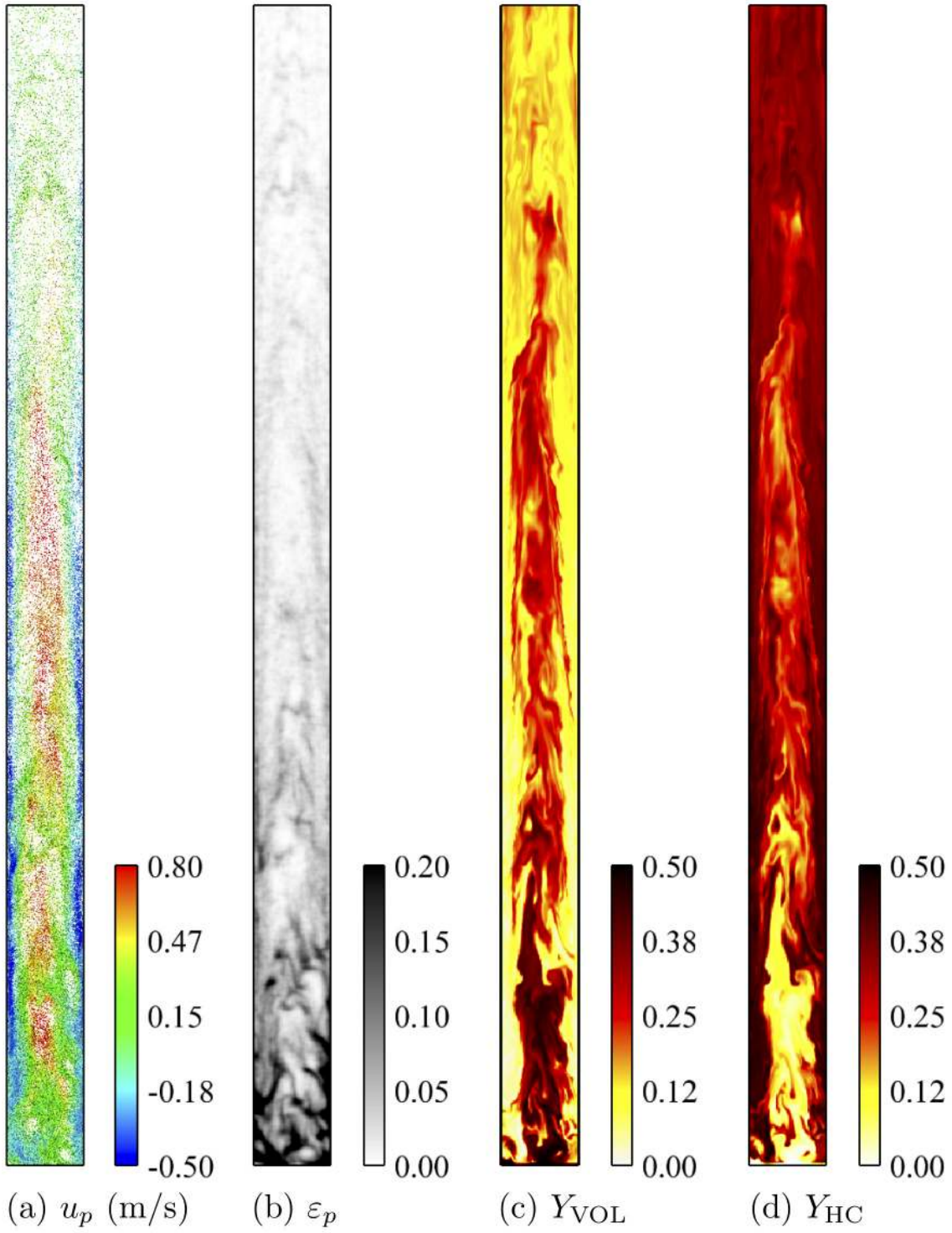

Figure 2: Instantaneous snapshot showing centerline planes of the three-dimensional reactor for $\mathcal{S}1$.

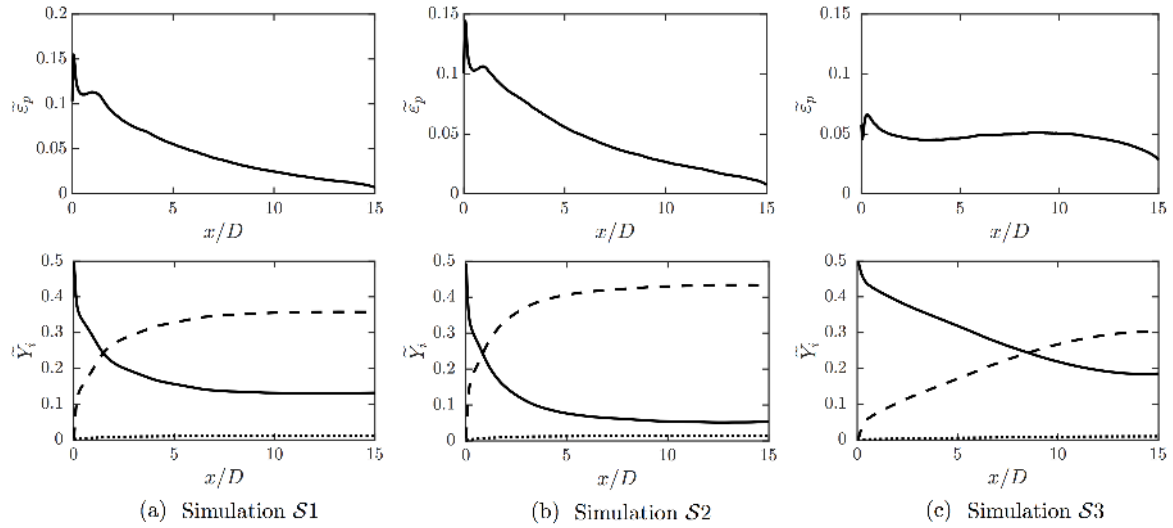

(a) Simulation $\mathcal{S}1$ (b) Simulation $\mathcal{S}2$ (c) Simulation $\mathcal{S}3$

Figure 3: Top row: Particle concentration profiles along the reactor height. Bottom row: Species mass fraction profiles along the reactor height: VOL (solid line) HC (dashed line) GAS (dotted line).

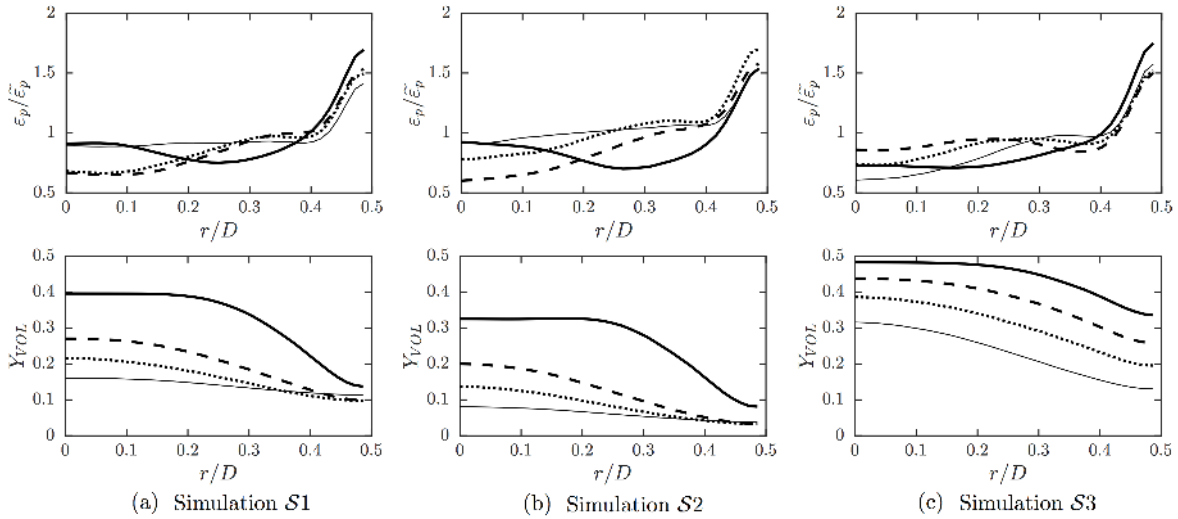

Figure 4: Top row: Radial profiles of the particle volume fraction normalized by the cross-sectional average at various reactor heights. Bottom row: Radial profiles of the volatile mass fractions at various reactor heights. $x/D = 1$ (thick line), 4 (thick dashed line), 7 (thick dotted line), and 12 (thin line).

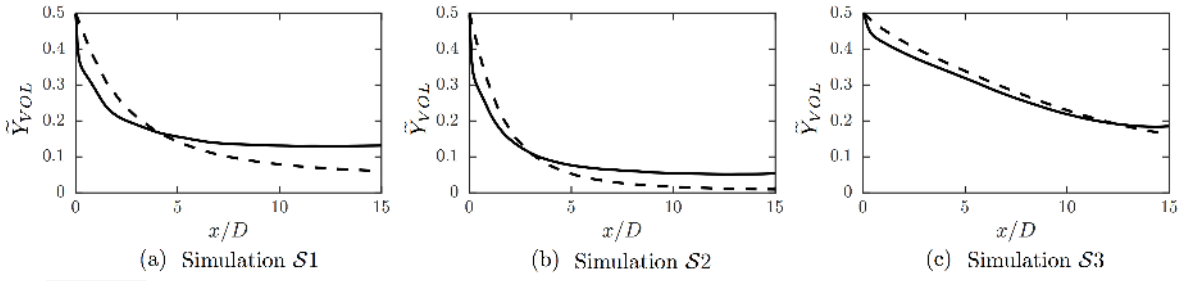

Figure 5: Comparison of axial volatile mass fraction profiles obtained from the three-dimensional simulations (solid line) and the CSTR-based engineering model (dashed line) with $\varepsilon_{f,(i)}$ obtained from the three-dimensional simulations for the configurations in Table 2.

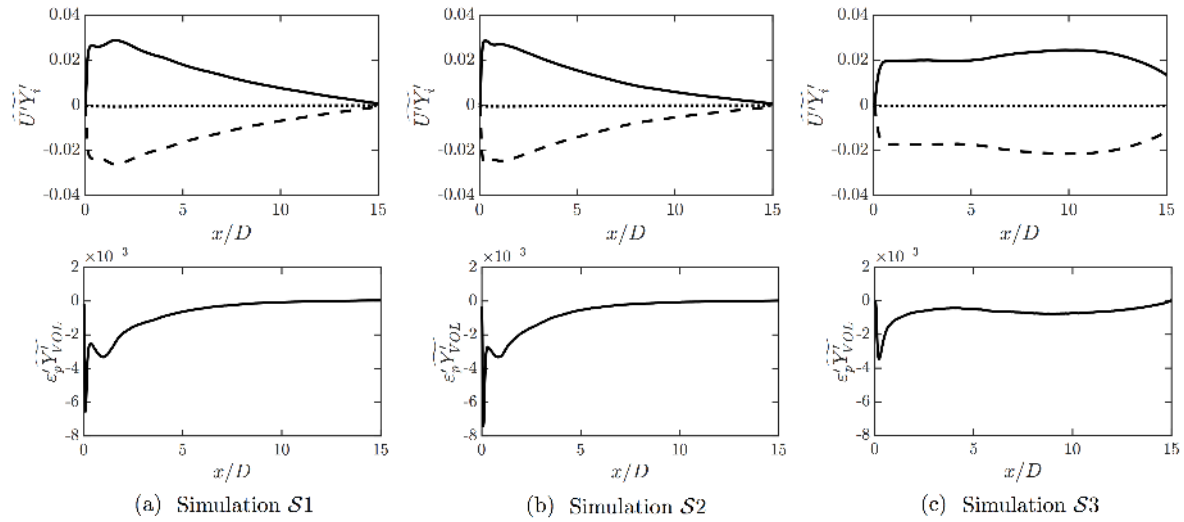

(a) Simulation $\mathcal{S}1$ (b) Simulation $\mathcal{S}2$ (c) Simulation $\mathcal{S}3$

Figure 6: Unclosed terms appearing in Eq. (26). Top row: $\widetilde{u'_f Y'_{\mathrm{VOL}}}$ (solid line), $\widetilde{u'_f Y'_{\mathrm{HC}}}$ (dashed line), and $\widetilde{u'_f Y'_{\mathrm{GAS}}}$ (thin solid line). Bottom row: $\widetilde{\varepsilon'_p Y'_{\mathrm{VOL}}}$.

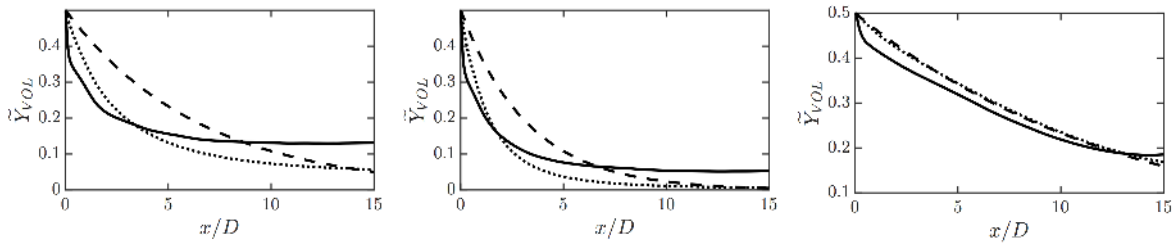

Figure 7: Volatile mass fraction profiles computed from the one-dimensional transport equations using the unclosed terms and volume fraction profile obtained from the three-dimensional simulation (solid line), neglecting the residual fluxes with $\widetilde{\varepsilon}_p = \overline{\varepsilon}_p$ (dashed line), and neglecting the residual fluxes with $\widetilde{\varepsilon}_p$ taken from the three-dimensional simulation (dotted line).

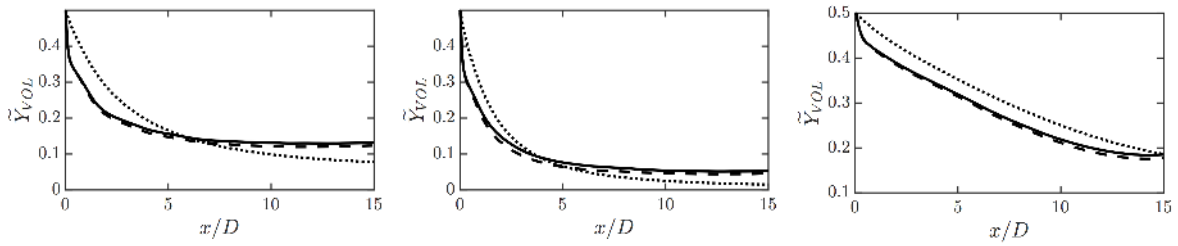

Figure 8: Volatile mass fraction profiles obtained from the three-dimensional simulations (solid line) and computed by solving Eq. (26) by 1) neglecting $\widetilde{\varepsilon_p' Y_{\mathrm{VOL}}'}$ while using $\widetilde{u_f' Y_{\mathrm{VOL}}'}$ obtained from the three-dimensional simulations (dashed line) and 2) neglecting $\widetilde{u_f' Y_{\mathrm{VOL}}'}$ while using $\widetilde{\varepsilon_p' Y_{\mathrm{VOL}}'}$ obtained from the three-dimensional simulations (dotted line).

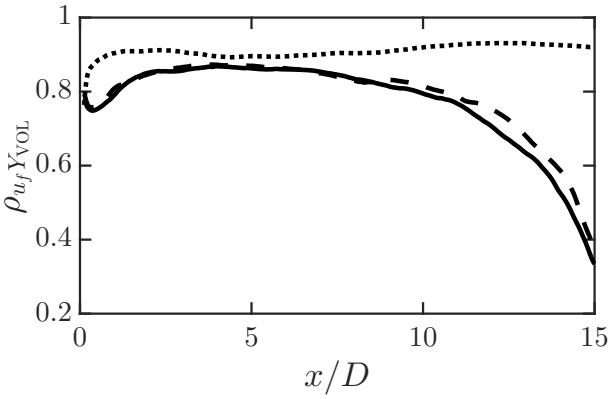

Figure 9: Correlation coefficient $\rho_{u_f,Y_{\mathrm{VOL}}}$ along the riser height for $\mathcal{S}1$ (solid line), $\mathcal{S}2$ (dashed line), and $\mathcal{S}3$ (dotted line).

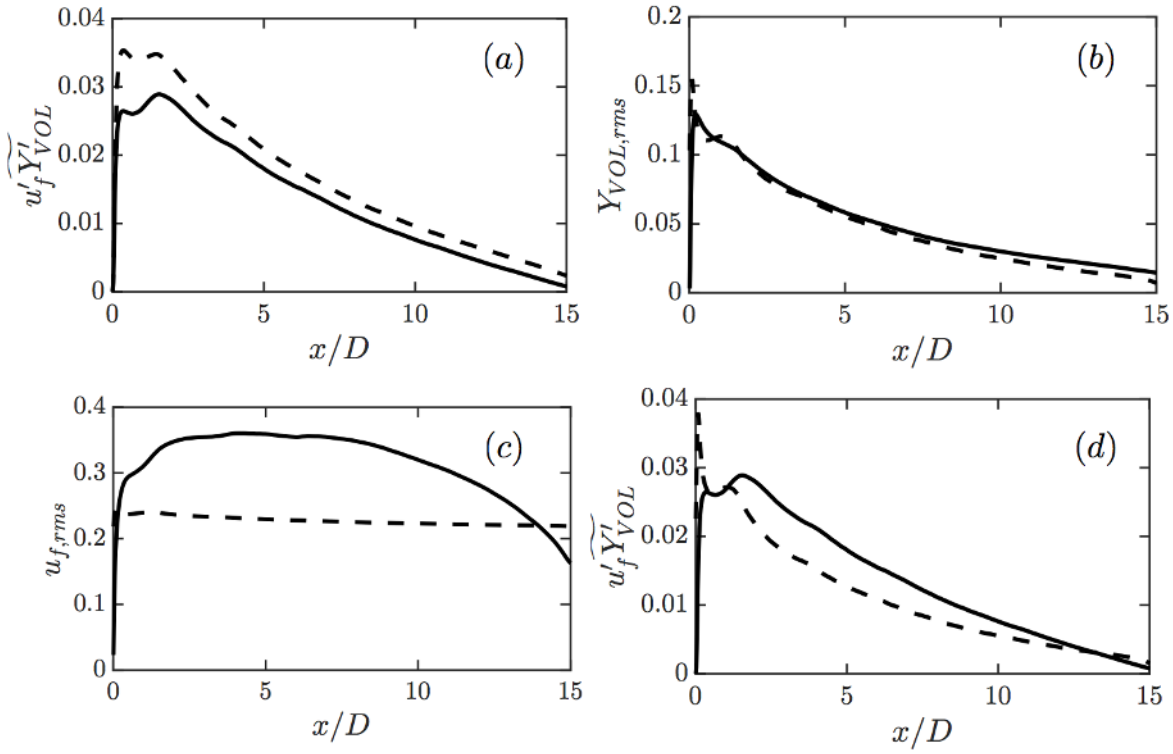

Figure 10: For simulation $\mathcal{S}1$, comparison of (a): $\widetilde{u'_f Y'_{\mathrm{VOL}}}$ (solid line) and $u_{\mathrm{f,RMS}} Y_{\mathrm{VOL,RMS}}$ (dashed line), (b): $Y_{\mathrm{VOL,RMS}}$ (solid line) and $\widetilde{\varepsilon}_p$ (dashed line), (c): $u_{\mathrm{f,RMS}}$ (solid line) and $\widetilde{u}_f$ (dashed line), (d): $\widetilde{u'_f Y'_{\mathrm{VOL}}}$ (solid line) and $\widetilde{u}_f \widetilde{\varepsilon}_p$ (dashed line).

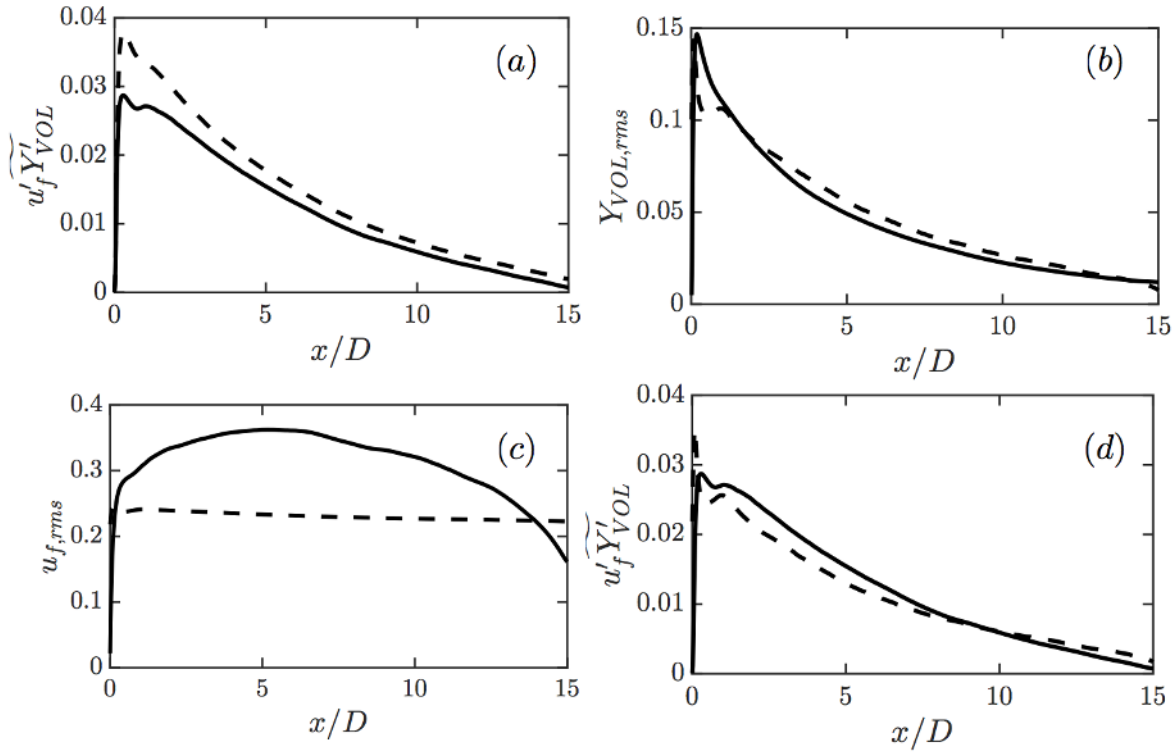

Figure 11: For simulation $\mathcal{S}2$, comparison of (a): $\widetilde{u'_f Y'_{\mathrm{VOL}}}$ (solid line) and $u_{\mathrm{f,RMS}} Y_{\mathrm{VOL,RMS}}$ (dashed line), (b): $Y_{\mathrm{VOL,RMS}}$ (solid line) and $\widetilde{\varepsilon}_p$ (dashed line), (c): $u_{\mathrm{f,RMS}}$ (solid line) and $\widetilde{u}_f$ (dashed line), (d): $\widetilde{u'_f Y'_{\mathrm{VOL}}}$ (solid line) and $\widetilde{u}_f \widetilde{\varepsilon}_p$ (dashed line).

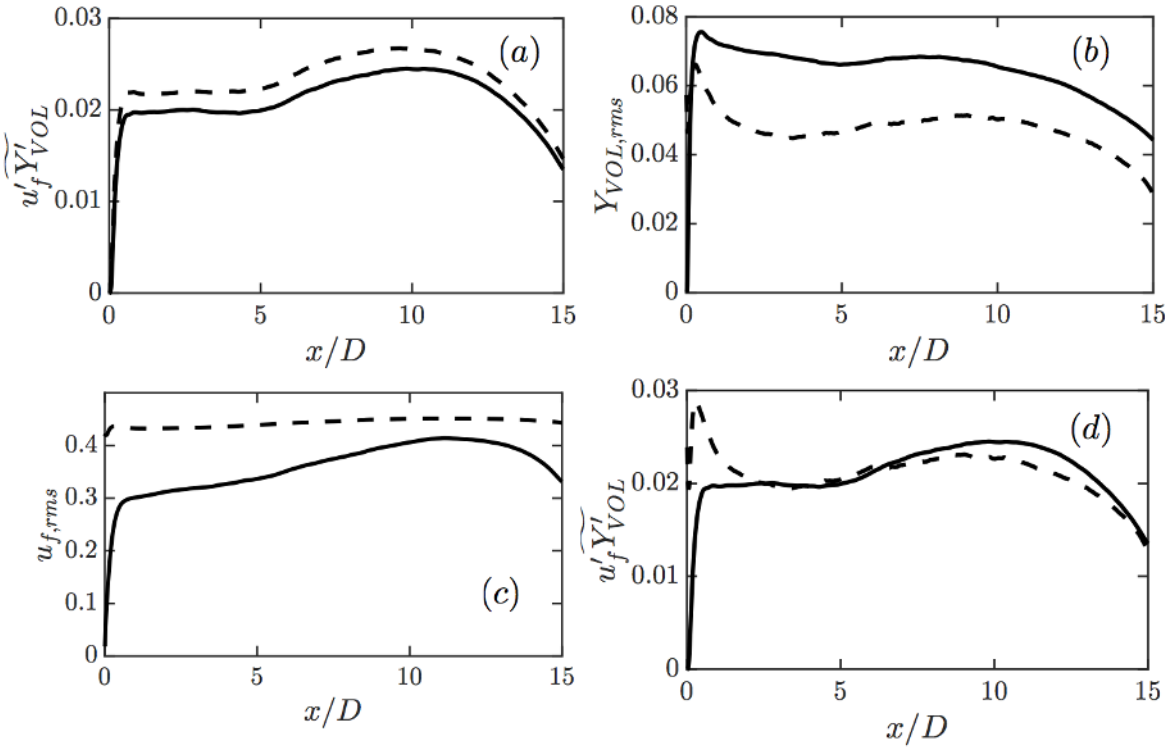

Figure 12: For simulation $\mathcal{S}3$, comparison of (a): $\widetilde{u'_f Y'_{\mathrm{VOL}}}$ (solid line) and $u_{\mathrm{f,RMS}} Y_{\mathrm{VOL,RMS}}$ (dashed line), (b): $Y_{\mathrm{VOL,RMS}}$ (solid line) and $\widetilde{\varepsilon}_p$ (dashed line), (c): $u_{\mathrm{f,RMS}}$ (solid line) and $\widetilde{u}_f$ (dashed line), (d): $\widetilde{u'_f Y'_{\mathrm{VOL}}}$ (solid line) and $\widetilde{u}_f \widetilde{\varepsilon}_p$ (dashed line).

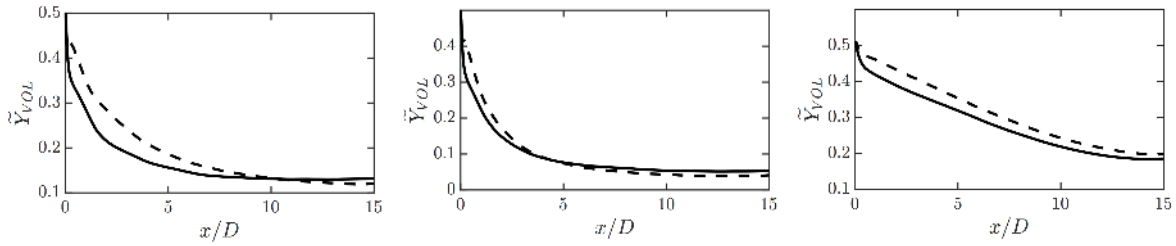

Figure 13: Comparison of volatile mass fraction profiles obtained from the three-dimensional simulations (solid line) and using the one-dimensional transport equation with the modeled $\widetilde{u'_f Y'_{\mathrm{VOL}}}$ (dotted line). (a) $\mathcal{S}1$, (b) $\mathcal{S}2$, and (c) $\mathcal{S}3$.

Table 1: Chemical compounds and their representative species. Elemental composition and molar mass chosen to match average conversion product distribution as listed in[61,62].

Compound class	Name	W [g/mol]	ν [-]	Representative species
Bio-oil volatile fraction	VOL	150	-1	*ad-hoc*[1]
Light gases	GAS	28	0.175	CO
Hydrocarbons	HC	92	1.575	Toluene
Inert medium	N_2	28	0	Nitrogen

[1] Elemental composition and molar mass chosen to match average conversion product distribution as listed in[61,62]

Table 2: Parameters for three-dimensional riser simulations.

Name	Units		Value	
Mesh $n_x \times n_y \times n_z$	-		$1024 \times 72 \times 72$	
Number of catalysts N_p	-		1.16×10^6	
Reactor diameter D	m		0.0102	
Height of the reactor L_x	m		0.1536	
Mean catalyst volume fraction	-		0.05	
Pressure	bar		21.7	
Temperature	°C		480	
Catalyst diameter d_p	μm		100	
Catalyst density ρ_p	kg/m^3		875	
Inflow composition Y_i	-		$0.5N_2$ 0.5VOL	
Simulation cases:		$\mathcal{S}1$(Base case)	$\mathcal{S}2$	$\mathcal{S}3$
Inlet velocity U	m/s	0.2	0.2	0.4
Rate constant k_0	s^{-1}	40	80	40

Table 3: Parameter to calculate the effective reaction rate constant.

	Units	$\mathcal{S}1$	$\mathcal{S}2$	$\mathcal{S}3$
$\mathcal{Y}_{\text{out}}$	-	0.050	0.005	0.158
$\mathcal{Y}^*_{\text{out}}$	-	0.131	0.054	0.185
k_0	s^{-1}	40	80	40
k_0^*	s^{-1}	23	39	35
$\mathcal{R}_{k_0}$	%	-43	-51	-13

Table 4: Da and Pe for different simulation cases.

	$\mathcal{S}1$	$\mathcal{S}2$	$\mathcal{S}3$
Da	2.4	4.8	1.2
Pe	1.7	1.8	9.2